

1 **SARS-CoV-2 spike D614G variant exhibits highly efficient replication and transmission**
2 **in hamsters**

3 Bobo Wing-Yee Mok¹, Conor J. Cremin¹, Siu-Ying Lau¹, Shaofeng Deng¹, Pin Chen¹, Anna
4 Jinxia Zhang¹, Andrew Chak-Yiu Lee¹, Honglian Liu¹, Siwen Liu¹, Timothy Ting-Leung Ng²,
5 Hiu-Yin Lao², Eddie Lam-Kwong Lee², Kenneth Siu-Sing Leung¹, Pui Wang¹, Kelvin Kai-
6 Wang To¹, Jasper Fuk-Woo Chan¹, Kwok-Hung Chan¹, Kwok-Yung Yuen¹, Gilman Kit-Hang
7 Siu² and Honglin Chen^{1*}

8

9

10 ¹Department of Microbiology and State Key Laboratory for Emerging Infectious Diseases, Li
11 Ka Shing Faculty of Medicine, The University of Hong Kong, Hong Kong SAR, China.

12 ²Department of Health Technology and Informatics, Faculty of Health and Social Sciences,
13 The Hong Kong Polytechnic University, Hong Kong SAR, China

14

15 ***Correspondence:** hlchen@hku.hk

16

17 **Summary**

18 SARS-CoV-2 causes disease varying in severity from asymptomatic infections to severe
19 respiratory distress and death in humans. The viral factors which determine transmissibility
20 and pathogenicity are not yet clearly characterized. We used the hamster infection model to
21 compare the replication ability and pathogenicity of five SARS-CoV-2 strains isolated from
22 early cases originating in Wuhan, China, in February, and infected individuals returning from
23 Europe and elsewhere in March 2020. The HK-13 and HK-95 isolates showed distinct
24 pathogenicity in hamsters, with higher virus titers and more severe pathological changes in the
25 lungs observed compared to other isolates. HK-95 contains a D614G substitution in the spike
26 protein and demonstrated higher viral gene expression and transmission efficiency in hamsters.
27 Intra-host diversity analysis revealed that further quasi species were generated during hamster
28 infections, indicating that strain-specific adaptive mutants with advantages in replication and
29 transmission will continue to arise and dominate subsequent waves of SARS-CoV-2
30 dissemination.

31

32 **Keywords:** Coronavirus, SARS-CoV-2, COVID-19, Spike, D614G, transmission, hamster

33

34 **Introduction**

35 A newly emerged β -coronavirus, SARS-CoV-2, which causes COVID-19 disease in humans,
36 attained cross species transmission through a process yet to be defined in detail (Andersen et
37 al., 2020; Wu et al., 2020; Zhou et al., 2020a). Human cases were first identified in Wuhan,
38 China, in December 2019 and SARS-CoV-2 subsequently disseminated worldwide leading to
39 the announcement of a global pandemic by the World Health Organization on March 11, 2020
40 (Mahase, 2020). More than 20 million laboratory-confirmed cases and over 700,000 deaths
41 have been recorded globally to date (<https://coronavirus.jhu.edu/map.html>) (Dong et al., 2020).
42 In contrast to SARS-CoV and MERS-CoV, a significant number of SARS-CoV-2 infections
43 are asymptomatic. However, in areas high virus activity a substantial portion of infections lead
44 to severe disease or death (Chen et al., 2020b). While aging and certain underlying medical
45 conditions may predispose individuals to increased severity of COVID-19 disease (Zhang et
46 al., 2020c), it is not clear if viral factors may also contribute to the variable pathogenicity of
47 SARS-CoV-2 in humans (Becerra-Flores and Cardozo, 2020). It is expected that SARS-CoV-
48 2 will continue to be transmitted among humans globally, leading to the emergence of more
49 phenotypic variants. It is therefore important to define the viral factors associated with
50 transmissibility and pathogenicity of SARS-CoV-2. Analysis of a mutant virus with a deletion
51 at the spike protein S1/S2 junction showed that the PRRA polybasic cleavage site is associated
52 with heightened pathogenicity in the model (Lau et al., 2020b). SARS-CoV-2 is of zoonotic
53 origin and is currently in the process of becoming more adapted to humans as it circulates and
54 acquires adaptative mutations. Different variants have already been identified among clinical
55 specimens and in cultured isolates (Gong et al., 2020; Su et al., 2020). Some deletion or
56 mutation variants may not be recognized by general sequencing protocols, for which the
57 readout only shows the dominant population in clinical specimens or cell culture samples, but
58 can be detected by more sensitive methods (Wong et al., 2020).

59 SARS-CoV-2 was first identified in China in December 2019 (Wu et al., 2020; Zhou et
60 al., 2020a). A response adopting aggressive control measures, including the lock down of a city
61 of 10 million people (Wuhan) and the wider Hubei Province (population: 56 million) in January
62 2020, significantly limited the further dissemination of the virus within China (Ji et al., 2020;
63 Lau et al., 2020a). SARS-CoV-2 has been efficiently transmitting among humans since it was
64 first recognized, according to studies from the early outbreak (Chan et al., 2020a; Liu et al.,
65 2020). Subsequent transmission of SARS-CoV-2 in Europe, the US and other countries has
66 resulted in more widespread human infections since March 2020. As more humans are exposed
67 to the SARS-CoV-2 virus, it is expected that more host adapted phenotypic variants of the virus

68 will emerge. It is important to determine whether some emerging variants may have the
69 potential to go on to become the dominant strain in the coming waves of circulation. Indeed, a
70 strain bearing a D614G mutation in the spike protein, first observed in January 2020 among
71 isolates from China and Europe, has since become the dominant population in the recent
72 transmissions occurring in Europe and the US (Korber et al., 2020). Studies using pseudo-
73 viruses containing spike genes derived from natural isolates have shown that variants harboring
74 D614G infect cells more effectively (Daniloski et al., 2020; Zhang et al., 2020b). Although
75 D614G is in the spike protein, the D614G variant is still susceptible to neutralization by
76 antibodies raised against strains lacking this mutation (Korber et al., 2020). To further
77 understand the properties of the D614G variant, we analyzed pathogenicity, virus replication
78 efficiency and the global transcriptome of the host response in the airways of SARS-CoV-2
79 D614G variant infected hamsters. Although it is not clear if the D614G variant causes more
80 severe disease in humans, our data showed that SARS-CoV-2 containing D614G replicates
81 more efficiently and causes more severe pathological changes in the lung tissues of infected
82 animals when compared to isolates lacking this mutation.

83

84 **Results**

85 **SARS-CoV-2 genomic variants exhibit variable pathogenicity in hamsters**

86 Five isolates were selected to study variability in the pathogenicity of SARS-CoV-2
87 strains and the host response to such variants in a hamster infection model. These strains
88 represent isolates from the early outbreak in China (HK-8, HK-13 and HK-15) and subsequent
89 outbreaks in Europe and elsewhere (HK-92 and HK-95) (Table S1). Phylogenetic analysis
90 revealed that these strains belonged to distinctive GISAID phylogenetic clades (**Figure S1**).
91 The sequences of these five isolates were compared with that of the index isolate (Wuhan-Hu-
92 1), characterized during the early outbreak in Wuhan city, China (Wu et al., 2020; Zhou et al.,
93 2020a), revealing a range of variations in the untranslated region and *Orf1a*, *Orf1b*, *Orf3*, *Orf8*,
94 *N* and *S* genes among strains (**Table 1**). HK-95 is an isolate characterized from a traveler
95 returning to Hong Kong from Egypt and carries a D614G substitution in the spike gene (**Figure**
96 **S1**). Hamsters are a highly susceptible model for studying SARS-CoV-2 infection, with disease
97 in hamsters closely simulating COVID-19 disease in humans (Chan et al., 2020b). Infection
98 progresses rapidly in hamsters, but infected animals then recover after about one-week of
99 infection. We infected hamsters with these five strains of SARS-CoV-2 and monitored disease
100 presentation for 5 days. All five isolates caused significant body weight loss compared to the
101 control group (**Figure 1A**). In SARS-CoV-2-infected hamsters, three major histopathological
102 changes were observed in lungs: various degrees of bronchial or bronchiolar inflammation
103 (bronchiolitis), lung parenchymal inflammatory damage (alveolitis) and pulmonary blood
104 vessel inflammation (vasculitis). These pathological changes were most severe at day 5 after
105 virus inoculation. The HK-13 and HK-95 isolates caused more extensive bronchiolar cell death,
106 diffuse alveolar space exudation and infiltration and lung consolidation, compared to HK-8
107 (**Figure 1B**). In our previous report, at day 4 post-infection (pi) with HK-001a virus, alveoli
108 had already started to show focal areas of cell proliferation indicating resolution of
109 inflammation (Chan et al., 2020b; Lau et al., 2020b). However, such indications of resolution
110 were not seen in HK-95- or HK-13-infected hamsters, even at day 5 post-infection, indicating
111 that the acute lung inflammation caused by both of these strains may last longer than that
112 triggered by infection with other SARS-CoV-2 strains.

113 **Differences in replication rates of SARS-CoV-2 isolates in infected hamsters**

114 Examination of virus titers in lung tissues and nasal washes at day 5 post-infection
115 showed that HK-13 and HK-95 replicate to significantly higher levels than the other three
116 isolates (**Figure 2A and S2**). We then analyzed viral gene expression in the lung tissues of
117 hamsters infected with different isolates using RNA-seq analysis. Consistent with the virus

118 titers, viral gene expression also showed a similar distribution between isolates when
119 comparing the average expression of all viral genes per isolate (black line) to viral titer profiles
120 (**Figure 2B**). Interestingly, the expression distribution between each of the viral genes for each
121 isolate is very similar across all isolates, with differences in overall expression being due to a
122 proportional change in expression across all genes. This indicates that the observed differences
123 in viral gene expression can be attributed to isolates maintaining different rates of replication.
124 These differences in replication suggest that some viral isolates may be more constrained by
125 host-specific factors and as such are unable to achieve an optimal rate of replication, as is seen
126 for HK-8. This also implies that individual isolates interact differently with their hosts during
127 the infection process. To assess if constraints to viral replication are reflected in the severity of
128 the host response induced by SARS-CoV-2 infection, we performed an initial characterization
129 of the hamster host response to infection.

130 **Differential expression of SARS-CoV-2 genes and host response in hamsters**

131 To further understand the global host response elicited by difference isolates, we
132 grouped the samples in a principal component analysis (PCA) (Figure 2C). In this PCA space,
133 we observed transcriptional perturbations along the two principal components, both account
134 for more than 25% of sample variation (Figure 2C). This analysis suggested unique expression
135 signatures in hamster host responses to infection with different SARS-CoV-2 isolates. In
136 addition, volcano plots show that viral isolates HK-13 and HK-95, which demonstrate higher
137 rates of replication than isolate HK-8, incited significant upregulation of host gene expression
138 compared to HK-8 (**Figure 3**). Unsurprisingly, the host responses provoked by HK-8 and HK-
139 15 were similar, as these isolates share a similar replication rate. These profiles suggest that
140 higher rates of SARS-CoV-2 replication are a significant driving factor in triggering host
141 responses, which may associate with greater disease severity in humans (Blanco-Melo et al.,
142 2020; Zhou et al., 2020b). However, the differential expression profile generated by comparing
143 HK-8 to HK-92 is similar to that of HK-8 vs HK-95. Since HK-92 has a considerably lower
144 replication efficiency than HK-95 in hamsters (**Figure 2**), this suggests that factors independent
145 of the replication of HK-92 are also involved in inducing the significant upregulation of host
146 gene expression seen here. This offers an explanation as to the close coordinate positioning of
147 HK-92 to HK-95 in our PCA analysis (**Figure 2C**), and why HK-13 is positioned further away,
148 despite possessing a similar replication rate to HK-95 (**Figure 2A and S2**). Our analysis has
149 made it clear that the upregulation of the host response is heavily dependent on the specific
150 viral SARS-CoV-2 isolate that is causing infection. Although viral replication is a significant

151 driver in stimulating the host response in hamsters, SARS-CoV-2 appears to have developed
152 replication-independent strategies to influence responses in infected hosts.

153 Hamsters have proven to be a useful live model for studying the dynamics of viral
154 infection and are now routinely used to assess SARS-CoV-2 pathogenesis (Chan et al., 2020b;
155 Lau et al., 2020b; Zhang et al., 2020a). However, the current annotation that is available to
156 describe gene functionality and perform network analysis in hamsters is limited. Therefore, we
157 opted to use the gene functional annotation of a well-defined animal model within close
158 evolutionary distance of the hamster. Our evolutionary analysis identified mice as being
159 suitably closely related to hamsters (**Figure S3**). Therefore, our gene enrichment analysis of
160 differentially expressed hamster-mouse gene orthologues using mouse Gene Ontology (GO)
161 annotation is anticipated to give a fair representation of the induced host response to SARS-
162 CoV-2, without enrichment of redundant hamster-specific processes. GO enrichment analysis
163 identified many functional groups corresponding to T-cell activation and chromatin remodeling
164 as being the networks most significantly upregulated by SARS-CoV-2 infection, regardless of
165 viral isolate used, when compared to samples from uninfected hamsters (**Figure 4**). Activation
166 of T-cells is indicative of upregulation of the adaptive immune response and the host's attempts
167 to restrict viral pathogenesis. The upregulation of chromatin remodeling pathways indicates
168 significant disruption to DNA architecture and an increase in nuclear repair processes,
169 potentially due to cellular stress caused by the SARS-CoV-2 virus during infection. We also
170 conducted GO enrichment analysis of differentially expressed genes in hamster lungs induced
171 by the various SARS-CoV-2 isolates, this time conducting comparisons to samples from HK-
172 95 hamster infections. Our result indicates that subverted gene networks are subject to strain
173 specific targeting processes by the more pathogenic strains of SARS-CoV-2, but not by HK-8
174 (**Figure S4**). Overall, the main effects of SARS-CoV-2 infection involved activation of the T
175 cell response and disruption of regulatory processes in the nuclear microenvironment of
176 infected cells.

177 **D614G variant demonstrates higher transmissibility in hamsters**

178 Surveillance of the evolution of SARS-CoV-2 during circulation in humans has
179 identified various mutations which may relate to the infectivity of virus (Chen et al., 2020a;
180 Korber et al., 2020) The spike D614G variant of SARS-CoV-2 has been the clearly dominant
181 population since March 2020, suggesting that it has enhanced infectivity in humans (Becerra-
182 Flores and Cardozo, 2020; Daniloski et al., 2020; Zhang et al., 2020b). We conducted an
183 experiment using the hamster model to examine if the transmission ability of the HK-95 strain,
184 which carries spike D614G, may be enhanced compared to two other isolates (HK-8 and HK-

185 13) which lack the D614G substitution (**Figure S5**). Notably, higher virus titers were found in
186 the lung and nasal turbinate tissues of recipient hamsters co-housed with HK-95-infected
187 hamsters than in those secondarily exposed to HK-8 or HK-13 (**Figure 5A**), which differs from
188 the direct infection experiment, where HK-13 and HK-95 demonstrated similar viral titers in
189 respiratory tissues (**Figure 2A and S2**). We did not examine if naive hamsters in the HK-95
190 group were infected at an earlier time point than those in other groups due to limited availability
191 of experimental animals. But given the higher viral titers in the lung and nasal turbinate tissues,
192 it is possible that hamsters co-housed with a HK-95-infected hamster were infected earlier than
193 those co-housed with hamsters infected with HK-8 or HK-13, and that this facilitated greater
194 virus replication in recipients. It is unclear how the D614G mutation affects virus replication.
195 The efficiency of spike protein cleavage is known to associate with coronavirus replication
196 (Hoffmann et al., 2020; Jaimes et al., 2020). We found that introduction of the D614G mutation
197 into the Wuhan-Hu-1 prototype sequence enhanced SARS-CoV-2 spike cleavage in cells
198 (**Figure 5B**). Since D614G is not located at either of the cleavage sites in the spike protein of
199 SARS-CoV-2, the molecular basis of this effect remains to be investigated. Taken together,
200 these results confirm that acquisition of D614G promotes SARS-CoV-2 infectivity in a
201 mammalian model of SARS-CoV-2 infection.

202 **Intra-host diversity in infected hamsters**

203 To examine intra-host diversity of the different SARS-CoV-2 strains, nasal washes
204 were collected from infected hamsters at days 3 and 5 post-infection and whole genome
205 sequencing conducted to determine the stability of the viral genome over the course of infection.
206 As inferred by Illumina sequencing data, even minor genome variant populations (i.e. variants
207 with frequency < 0.3) identified in the original inoculating strains (**Table 1**) remained present
208 after 5 days of infection (**Table S2**). Interestingly, some genome variants, which were absent
209 in the original strains, developed during hamster infection. The frequencies of these newly
210 arisen variants were generally higher at 5 dpi than at 3 dpi (**Table S2**). This trend of increase
211 implied that these new variants survive better in hamsters. Of note, there was no mixed
212 population observed in HK-95, either in the original isolate or in animals after infection, which
213 may indicate that the D614G variant has acquired a relatively stable genome constellation for
214 replication in mammals; this stability in both human isolates and hamster infections also further
215 supports the contention that hamsters are a suitable model for human SARS-CoV-2 infection.

216

217 Discussion

218 SARS-CoV-2 continues to transmit globally and since its emergence in December 2019
219 has caused more than 20 million laboratory confirmed infections and over 0.7 million deaths,
220 as of August 26 2020. Social distancing strategies have been adopted to slow down the
221 dissemination of virus, in hope that effective vaccines and therapeutics will be developed and
222 available soon enough to prevent further waves of transmission. More than seven months after
223 transmission in humans was first observed, various genetic variants of SARS-CoV-2 have
224 emerged and been analyzed but no clear evolutionary direction for SARS-CoV-2 is yet
225 apparent (Deng et al., 2020; Fauver et al., 2020; Forster et al., 2020; Sanchez-Pacheco et al.,
226 2020). Since the majority of people remain naive to this virus it is necessary to closely track
227 any potential changes in the pathogenic properties of SARS-CoV-2 variants along the course
228 of transmission. SARS-CoV-2 is of zoonotic origin and is expected to gain more adaptations
229 as it circulates in humans. Attenuated variants with deletions in the spike protein S1/S2 junction
230 and other regions have been detected in virus-infected cell cultures and in patient specimens
231 (Lau et al., 2020b; Wong et al., 2020). One variant containing D614G in the spike protein has
232 become the dominant population in many countries since March 2020 and is reported to infect
233 cells more efficiently *in vitro* (Daniloski et al., 2020; Li et al., 2020; Zhang et al., 2020b). To
234 understand if D614G variant virus may exhibit altered pathogenicity and transmissibility, we
235 compared 5 SARS-CoV-2 isolates obtained from Hong Kong returnees from Wuhan, China,
236 in February and travelers who had visited Europe and other countries after March 2020, using
237 the hamster infection model. We found that the D614G bearing strain, HK-95, replicates more
238 efficiently in the airways of infected hamsters in the lungs than strains lacking D614G (**Figure**
239 **2 and S2**). A contact transmission experiment showed that naive hamsters exposed to a HK-
240 95-infected hamster have higher titers of virus in their airways, suggesting that the D614G
241 variant is more highly transmissible than non-D614G SARS-CoV-2 strains (**Figure 5**).

242 Infection with SARS-CoV-2 can range from being asymptomatic to causing severe
243 disease and fatalities; it is not yet well understood which viral factors, together with host factors
244 and conditions, may determine pathogenicity in humans. Besides the insertion of a polybasic
245 cleavage PRRA motif at the S1/S2 junction of the spike protein, which clearly contributes to
246 increased virulence features, and was probably responsible for the initial SARS-CoV-2 cross
247 species transmission event (Andersen et al., 2020; Lau et al., 2020b), other virulence elements
248 are not well defined. The spike D614G variant, which was first recorded in January in China
249 (hCoV-19/Zhejiang/HZ103/2020; 24 January 2020) and shortly thereafter in Germany (hCoV-
250 19/Germany/BavPat1-Chvir929/2020; 28 January 2020), was found to have subsequently

251 become the dominant population in multiple countries, suggesting SARS-CoV-2 is adapting
252 to become more transmissible in humans. Host adaptation of an emerging virus in a naive
253 population is generally believed to involve the virus gaining more efficient replicative ability
254 while gradually decreasing its pathogenicity in the new host. It is not clear if the spike D614G
255 variant will drive SARS-CoV-2 towards this evolutionary pathway. The more pathogenic
256 features of the HK-95 strain, which carries the D614G substitution, observed in hamsters in
257 this study could be due to the high replication efficiency of this strain in animals, given that
258 hamsters are highly susceptible to SARS-CoV-2 infection. This is consistent with our
259 transcriptome analysis of lung tissues from infected hamsters, which revealed no significant
260 difference between host responses to infection with 614D or 614G strains (**Figure 4 and S4**).
261 However, the contact transmission experiment demonstrated that HK-95 exhibits higher
262 transmissibility to naive hamsters than HK-13 (**Figure 5**), despite these strains provoking
263 similar pathogenic effects and transcriptome profiles in infected hamsters (**Figure 1, 2, 4 and**
264 **S4**). If the spike D614G mutation is joined by other adaptive mutations as the virus further
265 circulates in humans, it may be postulated that a variant with the D614G substitution together
266 with a deletion in the polybasic cleavage site at the S1/S2 junction could arise, and if so, it may
267 present as a much less pathogenic version of SARS-CoV-2 in the aftermath of the COVID-19
268 pandemic. Nevertheless, human interventions, such as mass vaccination as soon as vaccines
269 are available, and preexisting immunity from prior infections are likely to drive the evolution
270 of variants that can evade host immunity.

271 The increased transmissibility of the D614G SARS-CoV-2 strain is likely due to its
272 higher replication ability. How the spike D614G mutation enhances virus replication and
273 consequently transmissibility has not been defined. We and others have shown that D614G
274 variant spike proteins are more efficiently cleaved into S1 and S2 subunits in cells (**Figure 5B**)
275 (Daniloski et al., 2020; Zhang et al., 2020b). Two synonymous mutations, 5'UTR-C241T and
276 *Orf1a*-C3037T, and one nonsynonymous mutation, *Orf1b*-P314L, are consistently linked in
277 D614G variant strains (**Table 1**). It remains to be investigated whether these mutations jointly
278 contribute to the enhanced replication ability of the HK-95 SARS-CoV-2 isolate. Of note,
279 *Orf1b*-P314L lies within the RNA-dependent RNA polymerase (RdRp) region, suggesting this
280 mutation may play a causative role on enhanced viral replication. Further studies, including
281 structural and functional analyses, will provide necessary information for understanding the
282 molecular basis underlying the D614G-associated SARS-CoV-2 phenotype.

283

284

285 **Acknowledgements**

286 The authors would like to thank Dr Jane Rayner for critical reading and editing of the
287 manuscript. This study is partly supported by the Theme-Based Research Scheme (T11/707/15)
288 and General Research Fund (17107019) of the Research Grants Council, Hong Kong Special
289 Administrative Region, China, and the Sanming Project of Medicine in Shenzhen, China (No.
290 SZSM201911014).

291

292 **Author contribution**

293 B.W.M. and H.C. designed the studies; B.W.M., C.J.C., S-Y.L., S.D., P.C., A.J.Z., A.C-Y.L.,
294 H.L., S.L., T.T-L.N., H-Y.L., E.L-K.L., K.S-S.L.,P.W. and K-H.C. performance experiments;
295 B.W.M., C.J.C., S-Y.L., A.J.Z., K.K-W.T., J.F-W.C, K-Y.Y., G.K-H.S., and H.C. analyzed the
296 data; B.W. M., C. J.C., G. K-H. S. and H.C. wrote the paper.

297 **Competing Interests statement**

298 The authors declare no conflict of interests.

299

300

301

302

303 **Materials and Methods**

304

305 **Virus**

306 The SARS-CoV-2 isolates HK-8 (MT835139), HK-13 (MT835140), HK-15 (MT835141),
307 HK-92 (MT835142) and HK-95 (MT835143) were isolated from specimens obtained from five
308 laboratory-confirmed COVID-19 patients using Vero E6 cells (ATCC; CRL-15786). All
309 experiments involving SARS-CoV-2 viruses were conducted in a Biosafety Level-3 laboratory.
310 For animal challenge, viral stocks were prepared after two serial passages of isolated virus in
311 Vero E6 cells in Dulbecco's Modified Eagle Medium (DMEM) (Thermo Fisher Scientific)
312 supplemented with 5% fetal bovine serum (Thermo Fisher Scientific), and 100 IU penicillin
313 G/ml and 100 ml streptomycin sulfate/ml (Thermo Fisher Scientific). Virus titers were then
314 determined by plaque assay using Vero E6 cells. Viral RNAs were also obtained from the
315 supernatants of infected cells and then isolated using the QIAamp RNA Viral kit (Qiagen) and
316 subjected to whole viral genome sequencing.

317

318 **Hamster infection**

319 Female golden Syrian hamsters, aged 8-9 weeks old, were obtained from the Laboratory
320 Animal Unit, the University of Hong Kong (HKU). All experiments were performed in a
321 Biosafety Level-3 animal facility at the LKS Faculty of Medicine, HKU. All animal studies
322 were approved by the Committee on the Use of Live Animals in Teaching and Research, HKU.
323 Virus stocks were diluted with phosphate-buffered saline (PBS) to 2×10^4 PFU/ml. Hamsters
324 were anesthetized with ketamine (150mg/kg) and xylazine (10 mg/mg) and then intranasally
325 inoculated with 50 ul of diluted virus stock containing 10^3 PFU of virus or 50 ul PBS (mock
326 infection control). Body weights were monitored daily for 5 days. Nasal washes were collected
327 from hamsters at 3 and 5 dpi. Total nucleic acid was extracted from 140 ul of sample fluid
328 using the QIAamp RNA Viral kit (Qiagen) and eluted with 30 ul of DEPC-treated water. Seven
329 ul RNA was used for reverse transcription using MultiScribe Reverse Transcriptase
330 (Thermofisher). cDNA was subsequently used for real-time qPCR using TB Green Premix Ex
331 Taq (Tli RNase H Plus) (Takara). Viral RNA from nasal washes was also used for whole viral
332 genome sequencing. Hamsters were euthanized at 5 dpi and lung tissues collected for
333 histopathology, determination of viral load and RNA sequencing.

334

335 **Viral load determination and histopathology**

336 Lung right lobes (superior, middle and inferior) were homogenized in 1 ml of PBS. After
337 centrifugation at 12,000 rpm for 10 min, the supernatant was harvested, and viral titers
338 determined by plaque assay using Vero E6 cells. Lung left superior lobes were fixed in 4 %
339 paraformaldehyde and then processed for paraffin embedding. The 4 µm tissue sections were
340 stained with haematoxylin and eosin for histopathological examination. Images were obtained
341 with an Olympus BX53 semi-motorized fluorescence microscope using cellSens imaging
342 software.

343

344 **RNA sequencing of hamster lung tissues**

345 Lung left inferior lobes from hamsters were cut into pieces and lysed using the RA1 lysis buffer
346 provided with the NucleoSpin® RNA Plus kit (Macherey-Nagel). RNA extraction was then
347 performed according to the manufacturer's instructions, including an on-column genomic
348 DNA digestion step. 1 µg of high-quality total RNA (RIN>8) was used for cDNA library
349 preparation with a KAPA mRNA HyperPrep Kit. The libraries were then denatured and diluted
350 to optimal concentration, before being sequenced on an Illumina NovaSeq 6000 in a 151bp
351 Paired-End format. RNA-seq data used in this study can be accessed in GEO under the
352 accession number GSE156005.

353

354 **Transmission experiment**

355 For each virus strain two hamsters were intranasally inoculated with 10³ PFU of virus. At
356 twenty-four hours post-infection (1 dpi), each infected donor hamster was transferred to a new
357 cage and co-housed with three naïve hamsters for 1 day. At 4 dpi, recipient hamsters were
358 euthanized, and lung and nasal turbinate tissues collected for determination of viral load.

359

360 **Differential expression (DE) analysis**

361 Sequencing reads were aligned to the merged golden hamster (*Mesocricetus_auratus*, V1.0,
362 ENSEMBL v100) and the SARS-CoV-2 (NCBI Accession: NC_045512.2) genomes using
363 STAR (Dobin et al., 2013). Read counts were extracted using the "--quantMode GeneCounts"
364 argument with STAR for each sample. Counts were used to perform differential expression
365 (DE) with DESeq2 (Love et al., 2014). DE thresholds required genes to have log2FoldChange
366 ≥ 1 and a p-adjusted value ≤ 0.05 to be considered for downstream characterization of gene
367 expression between conditions. Volcano plots were generated using the EnhancedVolcano R
368 package
369 ([www.bioconductor.org/packages/release/bioc/vignettes/EnhancedVolcano/inst/doc/Enhance](http://www.bioconductor.org/packages/release/bioc/vignettes/EnhancedVolcano/inst/doc/EnhancedVolcano.html)
370 [dVolcano.html](http://www.bioconductor.org/packages/release/bioc/vignettes/EnhancedVolcano/inst/doc/EnhancedVolcano.html)). Normalized viral gene counts were extracted from DESeq2 output. Boxplots
371 were generated with ggplot2 R package (Wickham, 2016). All analysis was performed through
372 R 4.0 with custom R script.

373

374 **Principal component analysis**

375 Log2FoldChange values for hamster DEGs for infections with each of the five isolates,
376 contrasted to samples from uninfected animals, were extracted from the results of DESeq2.
377 PCA analysis was performed on these values using the prcomp function from the stats R
378 package. Scatterplots of PCA outputs were generated using the ggplot2 R package.

379

380 **Evolutionary analysis**

381 The lack of annotation regarding mechanisms underlying the regulation of many biological
382 networks in hamsters required the determination of a well-annotated close relative from which
383 to infer the biological roles of differentially expressed genes in a species with a better
384 representation of the dynamics of the SARS-CoV-2 host response in humans. Evolutionary
385 analysis was performed in accordance to the protocol set by the author (Hall, 2013), using
386 MEGA X software. Briefly, IL6 gene sequence homologs were acquired through an extensive
387 search of the ENSEMBL (v100) database and their identity verified through nBLAST.
388 Sequences were aligned using MUSCLE, with positions with less than 95% coverage being
389 excluded (Edgar, 2004). The evolutionary history of IL6 was inferred using the Maximum
390 Likelihood method and Tamura 3-parameter model (Tamura, 1992).

391

392 **Gene set enrichment analysis (GSEA)**

393 Comprehensive lists of known mouse-hamster gene orthologues were compiled from the
394 BioMart database (Smedley et al., 2015). Differentially expressed hamster genes which were
395 identified to have a mouse orthologue form were retained from the orthologous gene list. These
396 lists of orthologues were matched to genes categorized into Gene Ontology (GO) biological
397 processes. The top 30 GO terms which were identified to have the most significant enrichment
398 ($FDR \leq 0.05$) across infected conditions were determined. A comparison between HK-95 and
399 non-D614G isolates was also conducted. Heatmaps of significant GO groups were generated
400 using the ComplexHeatmap R package (Gu et al., 2016).

401

402 **Whole viral genome sequencing:**

403 **Reverse transcription and viral genome amplification using multiplex PCR**

404 Viral RNA extracted from cell cultures and nasal washes was treated using the TURBO DNA-
405 free Kit (ThermoFisher Scientific) to remove residual host DNA, followed by synthesis of
406 single-strand cDNA using SuperScript IV reverse transcriptase (Invitrogen). The viral cDNA
407 was then enriched through multiplex tiling polymerase chain reaction (PCR), as described in
408 the ARTIC network (<https://artic.network/ncov-2019>) (Supplementary material).

409 **Nanopore sequencing of viral genome**

410 The input viral cDNA amplicons for individual samples were normalized to 5 ng, followed by
411 end-repairing and adapter ligation according to official 1D sequencing protocols (SQK-
412 LSK109, Oxford Nanopore). The libraries were sequenced on a Nanopore MinION device
413 using an R9.4.1 flow cell for 48 hours. Nanopore sequencing data were analyzed using a
414 modified Artic Network nCoV-2019 novel coronavirus bioinformatics protocol (Luo et al.,
415 2020) (Supplementary material).

416 **Illumina MiSeq sequencing of viral genome**

417 A total of 100 ng of multiplex PCR amplicons were subjected to library preparation and dual-
418 indexing using a KAPA HyperPrep Kit and a Unique Dual-Indexed Adapter Kit (Roche
419 Applied Science) in accordance with the manufacturer's instructions. Ligated libraries were
420 then enriched by 6-cycle PCR amplification, followed by purification and size selection using
421 AMPure XP beads (Beckman Coulter). The pooled libraries were sequenced using the MiSeq
422 Reagent Kit V2 Nano on an Illumina MiSeq System. The Illumina MiSeq sequencing reads
423 were then demultiplexed and mapped to the reference genome (accession number:

424 NC_0.45512.2) using Samtools v1.7. Variants were called with Freebayes v1.0.0
425 (<https://arxiv.org/abs/1207.3907>) with the haploid setting, with a minimum base quality and depth
426 of coverage of Q30 and 50x, respectively.

427 **Phylogenetic analysis**

428 To determine the phylogenetic placement of our strains in the global phylogeny of SARS-CoV-
429 2, a total of 100 SARS-CoV-2 genomes were downloaded from the GISAID severe acute
430 respiratory syndrome coronavirus 2 data hub (Elbe and Buckland-Merrett, 2017). A
431 phylogenetic tree was constructed with PhyML (v3.0) using the maximum likelihood algorithm.
432 A best-fit substitution model for phylogenetic analysis was created using the Akaike
433 information criterion, in which the general time reversible model with a fixed proportion of
434 invariable sites (+I) was selected (Guindon et al., 2010). Bootstrap replicates were set at 1000×,
435 and the maximum-likelihood phylogenetic tree was rooted on the earliest published genome of
436 SARS-CoV-2 (accession no.: NC_045512.2).

437

438 **References**

- 439 Andersen, K.G., Rambaut, A., Lipkin, W.I., Holmes, E.C., and Garry, R.F. (2020). The proximal origin of
440 SARS-CoV-2. *Nat Med* 26, 450-452.
- 441 Becerra-Flores, M., and Cardozo, T. (2020). SARS-CoV-2 viral spike G614 mutation exhibits higher case
442 fatality rate. *Int J Clin Pract*, e13525.
- 443 Blanco-Melo, D., Nilsson-Payant, B.E., Liu, W.C., Uhl, S., Hoagland, D., Moller, R., Jordan, T.X., Oishi, K.,
444 Panis, M., Sachs, D., *et al.* (2020). Imbalanced Host Response to SARS-CoV-2 Drives Development of
445 COVID-19. *Cell* 181, 1036-1045 e1039.
- 446 Chan, J.F., Yuan, S., Kok, K.H., To, K.K., Chu, H., Yang, J., Xing, F., Liu, J., Yip, C.C., Poon, R.W., *et al.*
447 (2020a). A familial cluster of pneumonia associated with the 2019 novel coronavirus indicating person-
448 to-person transmission: a study of a family cluster. *Lancet* 395, 514-523.
- 449 Chan, J.F., Zhang, A.J., Yuan, S., Poon, V.K., Chan, C.C., Lee, A.C., Chan, W.M., Fan, Z., Tsoi, H.W., Wen,
450 L., *et al.* (2020b). Simulation of the clinical and pathological manifestations of Coronavirus Disease
451 2019 (COVID-19) in golden Syrian hamster model: implications for disease pathogenesis and
452 transmissibility. *Clin Infect Dis*.
- 453 Chen, J., Wang, R., Wang, M., and Wei, G.W. (2020a). Mutations Strengthened SARS-CoV-2 Infectivity.
454 *J Mol Biol* S0022-2836, 30456-30453.
- 455 Chen, N., Zhou, M., Dong, X., Qu, J., Gong, F., Han, Y., Qiu, Y., Wang, J., Liu, Y., Wei, Y., *et al.* (2020b).
456 Epidemiological and clinical characteristics of 99 cases of 2019 novel coronavirus pneumonia in Wuhan,
457 China: a descriptive study. *Lancet* 395, 507-513.
- 458 Daniloski, Z., Guo, X., and Sanjana, N.E. (2020). The D614G mutation in SARS-CoV-2 Spike increases
459 transduction of multiple human cell types. *bioRxiv*.
- 460 Deng, X., Gu, W., Federman, S., du Plessis, L., Pybus, O.G., Faria, N., Wang, C., Yu, G., Bushnell, B., Pan,
461 C.Y., *et al.* (2020). Genomic surveillance reveals multiple introductions of SARS-CoV-2 into Northern
462 California. *Science* 369, 582-587.
- 463 Dobin, A., Davis, C.A., Schlesinger, F., Drenkow, J., Zaleski, C., Jha, S., Batut, P., Chaisson, M., and
464 Gingeras, T.R. (2013). STAR: ultrafast universal RNA-seq aligner. *Bioinformatics* 29, 15-21.
- 465 Dong, E., Du, H., and Gardner, L. (2020). An interactive web-based dashboard to track COVID-19 in real
466 time. *Lancet Infect Dis* 20, 533-534.

467 Edgar, R.C. (2004). MUSCLE: a multiple sequence alignment method with reduced time and space
468 complexity. *BMC Bioinformatics* 5, 113.

469 Elbe, S., and Buckland-Merrett, G. (2017). Data, disease and diplomacy: GISAID's innovative
470 contribution to global health. *Glob Chall* 1, 33-46.

471 Fauver, J.R., Petrone, M.E., Hodcroft, E.B., Shioda, K., Ehrlich, H.Y., Watts, A.G., Vogels, C.B.F., Brito,
472 A.F., Alpert, T., Muyombwe, A., *et al.* (2020). Coast-to-Coast Spread of SARS-CoV-2 during the Early
473 Epidemic in the United States. *Cell* 181, 990-996 e995.

474 Forster, P., Forster, L., Renfrew, C., and Forster, M. (2020). Phylogenetic network analysis of SARS-
475 CoV-2 genomes. *Proc Natl Acad Sci U S A* 117, 9241-9243.

476 Gong, Y.N., Tsao, K.C., Hsiao, M.J., Huang, C.G., Huang, P.N., Huang, P.W., Lee, K.M., Liu, Y.C., Yang,
477 S.L., Kuo, R.L., *et al.* (2020). SARS-CoV-2 genomic surveillance in Taiwan revealed novel ORF8-deletion
478 mutant and clade possibly associated with infections in Middle East. *Emerg Microbes Infect*, 1-37.

479 Gu, Z., Eils, R., and Schlesner, M. (2016). Complex heatmaps reveal patterns and correlations in
480 multidimensional genomic data. *Bioinformatics* 32, 2847-2849.

481 Guindon, S., Dufayard, J.F., Lefort, V., Anisimova, M., Hordijk, W., and Gascuel, O. (2010). New
482 algorithms and methods to estimate maximum-likelihood phylogenies: assessing the performance of
483 PhyML 3.0. *Syst Biol* 59, 307-321.

484 Hall, B.G. (2013). Building phylogenetic trees from molecular data with MEGA. *Mol Biol Evol* 30, 1229-
485 1235.

486 Hoffmann, M., Kleine-Weber, H., and Pohlmann, S. (2020). A Multibasic Cleavage Site in the Spike
487 Protein of SARS-CoV-2 Is Essential for Infection of Human Lung Cells. *Mol Cell* 78, 779-784 e775.

488 Jaimes, J.A., Millet, J.K., and Whittaker, G.R. (2020). Proteolytic Cleavage of the SARS-CoV-2 Spike
489 Protein and the Role of the Novel S1/S2 Site. *iScience* 23, 101212.

490 Ji, T., Chen, H.L., Xu, J., Wu, L.N., Li, J.J., Chen, K., and Qin, G. (2020). Lockdown contained the spread
491 of 2019 novel coronavirus disease in Huangshi city, China: Early epidemiological findings. *Clin Infect*
492 *Dis*.

493 Korber, B., Fischer, W.M., Gnanakaran, S., Yoon, H., Theiler, J., Abfalterer, W., Hengartner, N., Giorgi,
494 E.E., Bhattacharya, T., Foley, B., *et al.* (2020). Tracking Changes in SARS-CoV-2 Spike: Evidence that
495 D614G Increases Infectivity of the COVID-19 Virus. *Cell* 182, 812-827.

496 Lau, H., Khosrawipour, V., Kocbach, P., Mikolajczyk, A., Schubert, J., Bania, J., and Khosrawipour, T.
497 (2020a). The positive impact of lockdown in Wuhan on containing the COVID-19 outbreak in China. *J*
498 *Travel Med* 27.

499 Lau, S.Y., Wang, P., Mok, B.W., Zhang, A.J., Chu, H., Lee, A.C., Deng, S., Chen, P., Chan, K.H., Song, W.,
500 *et al.* (2020b). Attenuated SARS-CoV-2 variants with deletions at the S1/S2 junction. *Emerg Microbes*
501 *Infect* 9, 837-842.

502 Li, Q., Wu, J., Nie, J., Zhang, L., Hao, H., Liu, S., Zhao, C., Zhang, Q., Liu, H., Nie, L., *et al.* (2020). The
503 Impact of Mutations in SARS-CoV-2 Spike on Viral Infectivity and Antigenicity. *Cell* 182, 30877-
504 30871.

505 Liu, Y., Ning, Z., Chen, Y., Guo, M., Liu, Y., Gali, N.K., Sun, L., Duan, Y., Cai, J., Westerdahl, D., *et al.*
506 (2020). Aerodynamic analysis of SARS-CoV-2 in two Wuhan hospitals. *Nature* 582, 557-560.

507 Love, M.I., Huber, W., and Anders, S. (2014). Moderated estimation of fold change and dispersion for
508 RNA-seq data with DESeq2. *Genome Biol* 15, 550.

509 Luo, R., Wang, C.-L., Yat-Sing, W., Tang, C.-I., Liu, C.-M., Chi-Ming, L., and Lam, T.-W. (2020). Exploring
510 the limit of using a deep neural network on pileup data for germline variant calling. *Nature* 2,
511 pages220–227.

512 Mahase, E. (2020). Covid-19: WHO declares pandemic because of "alarming levels" of spread, severity,
513 and inaction. *BMJ* 368, m1036.

514 Sanchez-Pacheco, S.J., Kong, S., Pulido-Santacruz, P., Murphy, R.W., and Kubatko, L. (2020). Median-
515 joining network analysis of SARS-CoV-2 genomes is neither phylogenetic nor evolutionary. *Proc Natl*
516 *Acad Sci U S A* 117, 12518-12519.

517 Smedley, D., Haider, S., Durinck, S., Pandini, L., Provero, P., Allen, J., Arnaiz, O., Awedh, M.H., Baldock,
518 R., Barbiera, G., *et al.* (2015). The BioMart community portal: an innovative alternative to large,
519 centralized data repositories. *Nucleic Acids Res* 43, W589-598.

520 Su, Y.C.F., Anderson, D.E., Young, B.E., Linster, M., Zhu, F., Jayakumar, J., Zhuang, Y., Kalimuddin, S.,
521 Low, J.G.H., Tan, C.W., *et al.* (2020). Discovery and Genomic Characterization of a 382-Nucleotide
522 Deletion in ORF7b and ORF8 during the Early Evolution of SARS-CoV-2. *mBio* 11.

523 Tamura, K. (1992). Estimation of the number of nucleotide substitutions when there are strong
524 transition-transversion and G+C-content biases. *Mol Biol Evol* 9, 678-687.

525 Wickham, H. (2016). *ggplot2: Elegant Graphics for Data Analysis*. pringer-Verlag New York.

526 Wong, Y.C., Lau, S.Y., Wang To, K.K., Mok, B.W.Y., Li, X., Wang, P., Deng, S., Woo, K.F., Du, Z., Li, C., *et*
527 *al.* (2020). Natural transmission of bat-like SARS-CoV-2PRRA variants in COVID-19 patients. *Clin Infect*
528 *Dis*.

529 Wu, F., Zhao, S., Yu, B., Chen, Y.M., Wang, W., Song, Z.G., Hu, Y., Tao, Z.W., Tian, J.H., Pei, Y.Y., *et al.*
530 (2020). A new coronavirus associated with human respiratory disease in China. *Nature* 579, 265-269.

531 Zhang, A.J., Lee, A.C., Chu, H., Chan, J.F., Fan, Z., Li, C., Liu, F., Chen, Y., Yuan, S., Poon, V.K., *et al.*
532 (2020a). SARS-CoV-2 infects and damages the mature and immature olfactory sensory neurons of
533 hamsters. *Clin Infect Dis*.

534 Zhang, L., Jackson, C.B., Mou, H., Ojha, A., Rangarajan, E.S., Izard, T., Farzan, M., and Choe, H. (2020b).
535 The D614G mutation in the SARS-CoV-2 spike protein reduces S1 shedding and increases infectivity.
536 *bioRxiv*.

537 Zhang, X., Tan, Y., Ling, Y., Lu, G., Liu, F., Yi, Z., Jia, X., Wu, M., Shi, B., Xu, S., *et al.* (2020c). Viral and
538 host factors related to the clinical outcome of COVID-19. *Nature* 583, 437-440.

539 Zhou, P., Yang, X.L., Wang, X.G., Hu, B., Zhang, L., Zhang, W., Si, H.R., Zhu, Y., Li, B., Huang, C.L., *et al.*
540 (2020a). A pneumonia outbreak associated with a new coronavirus of probable bat origin. *Nature* 579,
541 270-273.

542 Zhou, Z., Ren, L., Zhang, L., Zhong, J., Xiao, Y., Jia, Z., Guo, L., Yang, J., Wang, C., Jiang, S., *et al.* (2020b).
543 Heightened Innate Immune Responses in the Respiratory Tract of COVID-19 Patients. *Cell Host*
544 *Microbe* 27, 883-890 e882.

545

546 **Figure legends**

547 **Figure 1. Body weight and histopathological changes in golden Syrian hamsters**

548 **challenged with different strains of SARS-CoV-2.** (A) Body weight change in hamsters after

549 viral infection. Body weights of virus-infected and mock-infected hamsters (n=3) were
550 monitored daily for 5 days. Data are shown as the mean \pm SD percentages of the starting weight.

551 (B) Haematoxylin and eosin (H&E) staining of lung sections from SARS-CoV-2 (HK-8, HK-
552 13 and HK-95) infected hamsters, collected at 5 days post-infection (dpi). The lower

553 photographs depict higher magnification images of the regions denoted by circles in upper

554 photographs (upper photographs = 500x magnification). **HK-8:** Upper panel shows patchy

555 inflammatory damage with areas showing peribronchiolar and perivascular infiltration, blood

556 vessel congestion and areas of alveolar wall thickening, while alveolar exudation and

557 infiltration were not apparent. Lower panel: (1) bronchiolar luminal exudation with cell debris

558 (arrows), surrounding alveolar wall infiltration (arrowhead); (2) a small sized blood vessel

559 shows perivascular and endothelial infiltration (arrows), but the surrounding alveolar space

560 shows no infiltration or exudation (arrowhead); (3) alveolar wall capillary congestion and

561 moderate infiltration (arrow). **HK-13:** Upper panel shows diffuse lung tissue inflammatory

562 damage with massive alveolar space infiltration and exudation; perivascular infiltration and

563 endothelial infiltration can be observed in all blood vessels in this lung section. Lower panel:

564 (1) mild bronchiolar luminal exudation with cell debris (arrows); (2) a large blood vessel shows

565 severe endothelial infiltration and vessel wall infiltration (arrows) and surrounding alveolar

566 space infiltration and exudation (arrowheads); (3) alveolar structure destroyed by septal edema

567 and alveolar space infiltration and fluid exudation (arrows). **HK-95:** Upper panel shows diffuse

568 lung tissue damage with massive alveolar space exudation and infiltration; all blood vessels in

569 the field show perivascular infiltration and endothelial infiltration. A moderate degree of

570 bronchiolar epithelial cell death and luminal exudation is seen. Lower panel: (1) bronchiolar

571 luminal exudation with cell debris (arrow); (2) a medium sized blood vessel shows severe

572 endothelial infiltration and vessel wall infiltration (arrows), with alveolar space infiltration in

573 alveoli surrounding the vessel (arrowheads); (3) alveolar structure has reduced cellularity but

574 shows alveolar septal edema and alveolar space fluid exudation (arrows).

575

576 **Figure 2. Viral replication and transcriptome response to different SARS-CoV-2 isolates**

577 **in hamster lungs.** (A) Virus replication in hamsters infected with different SARS-CoV-2

578 isolates. Three to seven hamsters per group were euthanized on day 5 post-infection for viral

579 titration. Virus titers in lungs were determined by plaque assays (PFU/ml) and displayed as

580 mean (\pm SEM). (B) Average viral gene expression in samples from hamsters infected with each
581 isolate. Horizontal black lines indicate the overall mean of average expression values for viral
582 genes per isolate. (C) Transcriptome response to different SARS-CoV-2 isolates in hamster
583 lungs. Principal component analysis of global transcription profiles of significantly expressed
584 host genes for infections with each isolate, compared to uninfected conditions. Individual data
585 points and means \pm SEM are also shown. Statistical significance was calculated by Mann
586 Whitney Wilcoxon Test; * denotes $p < 0.05$, ** denotes $p < 0.005$ and ns denotes *non-significant*.
587

588 **Figure 3. Volcano plots comparing differentially expressed genes (DEGs) in HK-8-**
589 **infected hamster lungs to those in hamsters infected with HK-13, HK-15, HK-92 or HK-**
590 **95.** DEGs: $\log_2\text{FoldChange} \geq 1$ and p-adjusted value ≤ 0.05 .

591

592 **Figure 4. Differential gene expression in SARS-CoV-2 infection.**

593 Heatmap depicting the expression levels of enriched gene sets in lungs collected from hamsters
594 infected with the indicated viruses at 5 dpi. Gene enrichment was performed on differentially
595 expressed genes identified in comparisons between infections with each of the 5 different
596 SARS-CoV-2 isolates and uninfected controls. DEGs that were identified as hamster–mouse
597 orthologues were extracted and matched to gene members of mouse GO biological processes.
598 The top 30 GO biological processes with significant enrichment ($\text{FDR} \leq 0.05$) across infected
599 conditions are displayed.

600

601 **Figure 5. D614G enhances efficiency of spike protein cleavage and transmission of SARS-**
602 **CoV-2 isolates in hamsters.**

603 (A) Transmission of SARS-CoV-2 isolates. For each isolate, two groups of three naïve
604 hamsters were each co-housed with one inoculated donor on day 1 post-infection. Viral loads
605 (PFU/ml) in lungs and nasal turbinates of naïve contact hamsters ($n=6$ per isolate) at 3 days
606 after exposure are shown. Data are presented as individual data points and means \pm SEM.
607 Statistical significance was calculated by Mann Whitney Wilcoxon Test; (*) p value < 0.05 , ns
608 – not significant. (B) The human codon-optimized spike gene of Wuhan-Hu-1 SARS-CoV-2
609 was cloned into the Flag-tagged-pCAGEN vector. A pCAGEN-S-D614G-Flag mutant was
610 constructed using a QuikChange site-directed mutagenesis kit (Agilent) according to the
611 standard protocol. Protein expression and cleavage in transfected HEK293T-ACE2 cells was

612 demonstrated with western blotting. Rabbit anti-Spike RBD was used to detect the spike and
613 S1 proteins, and mouse anti-Flag M2 to detect S2 protein (Supplementary materials).

614

615

616

617

Figure 1

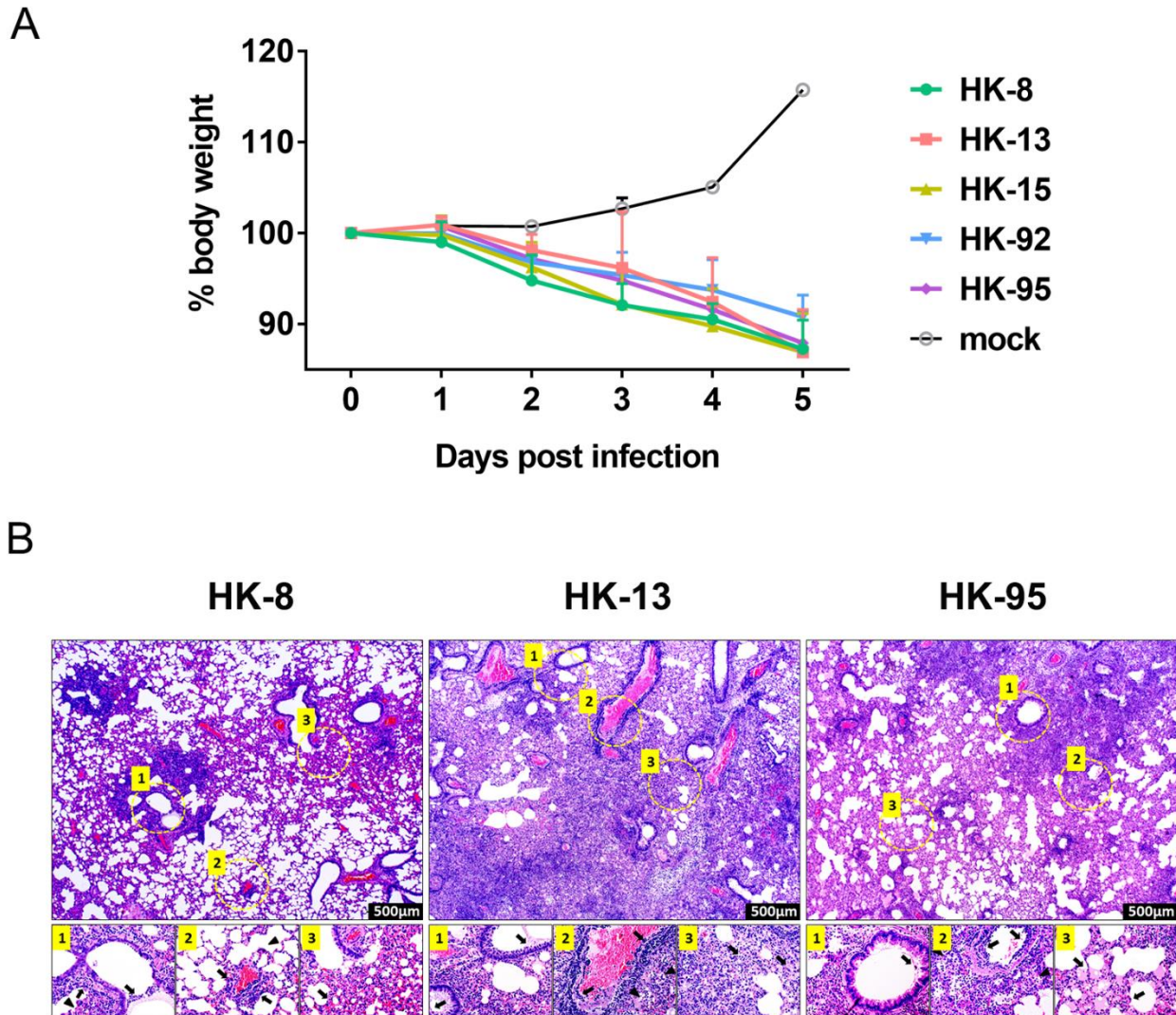


Figure 2

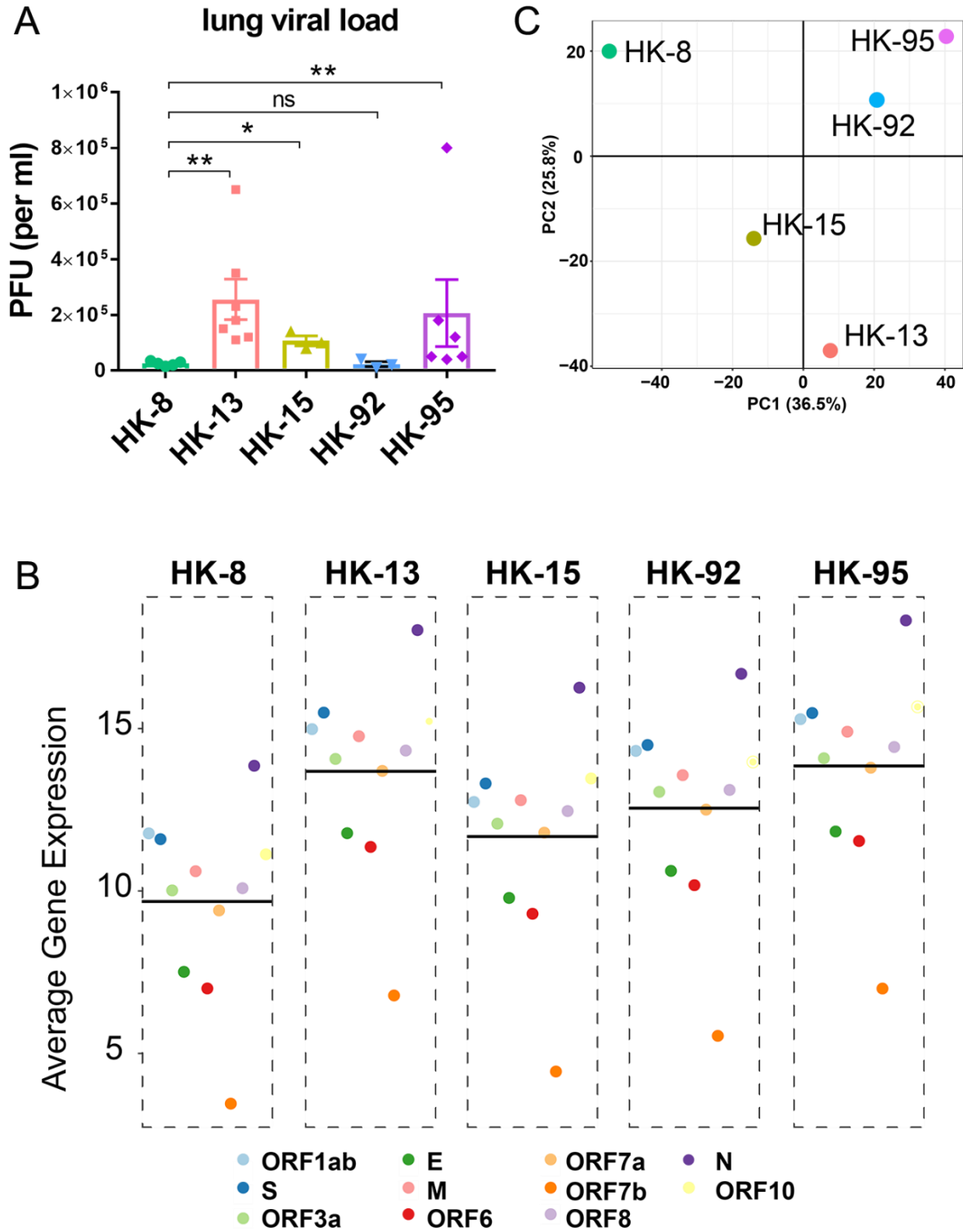


Figure 3

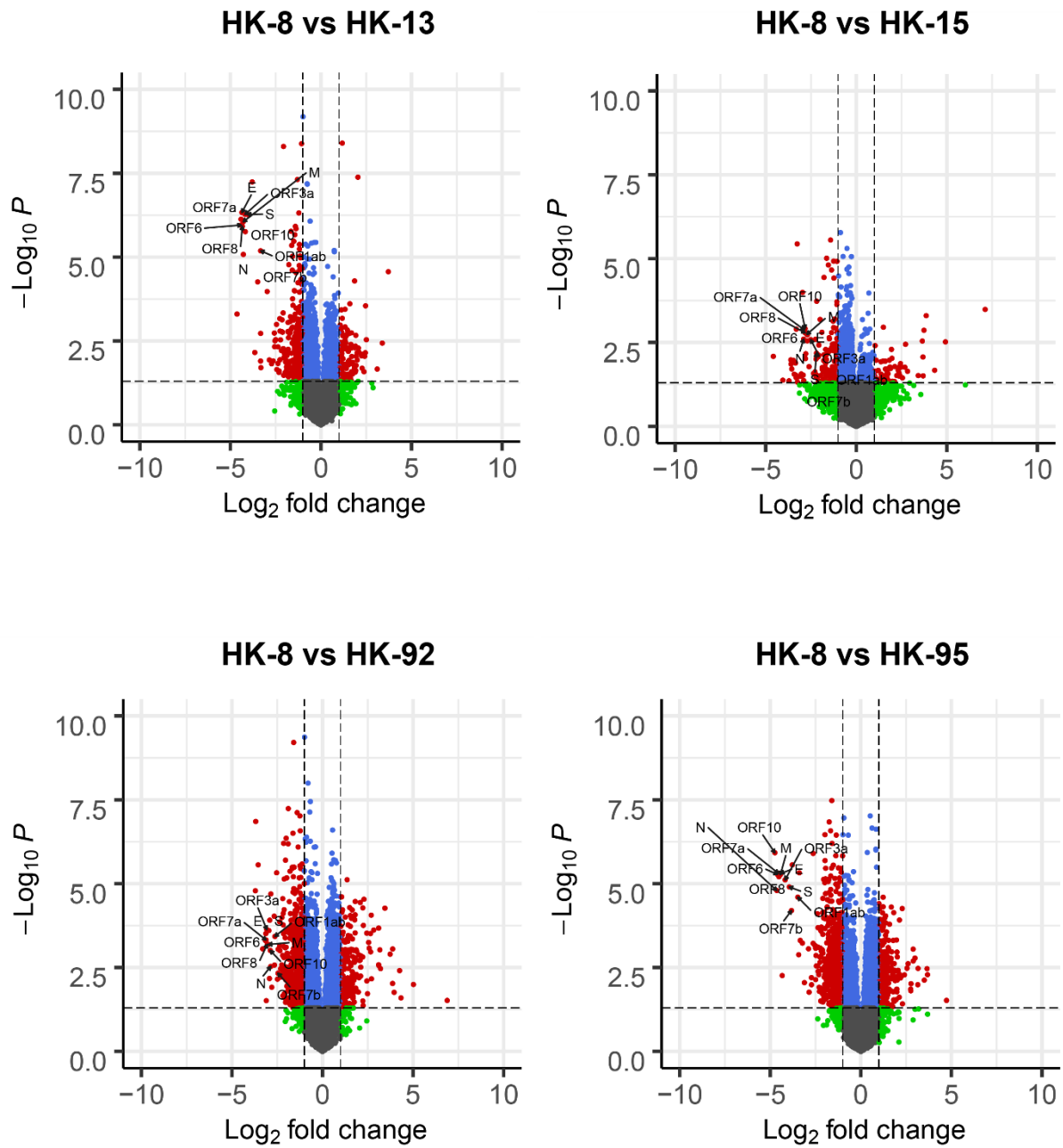


Figure 4

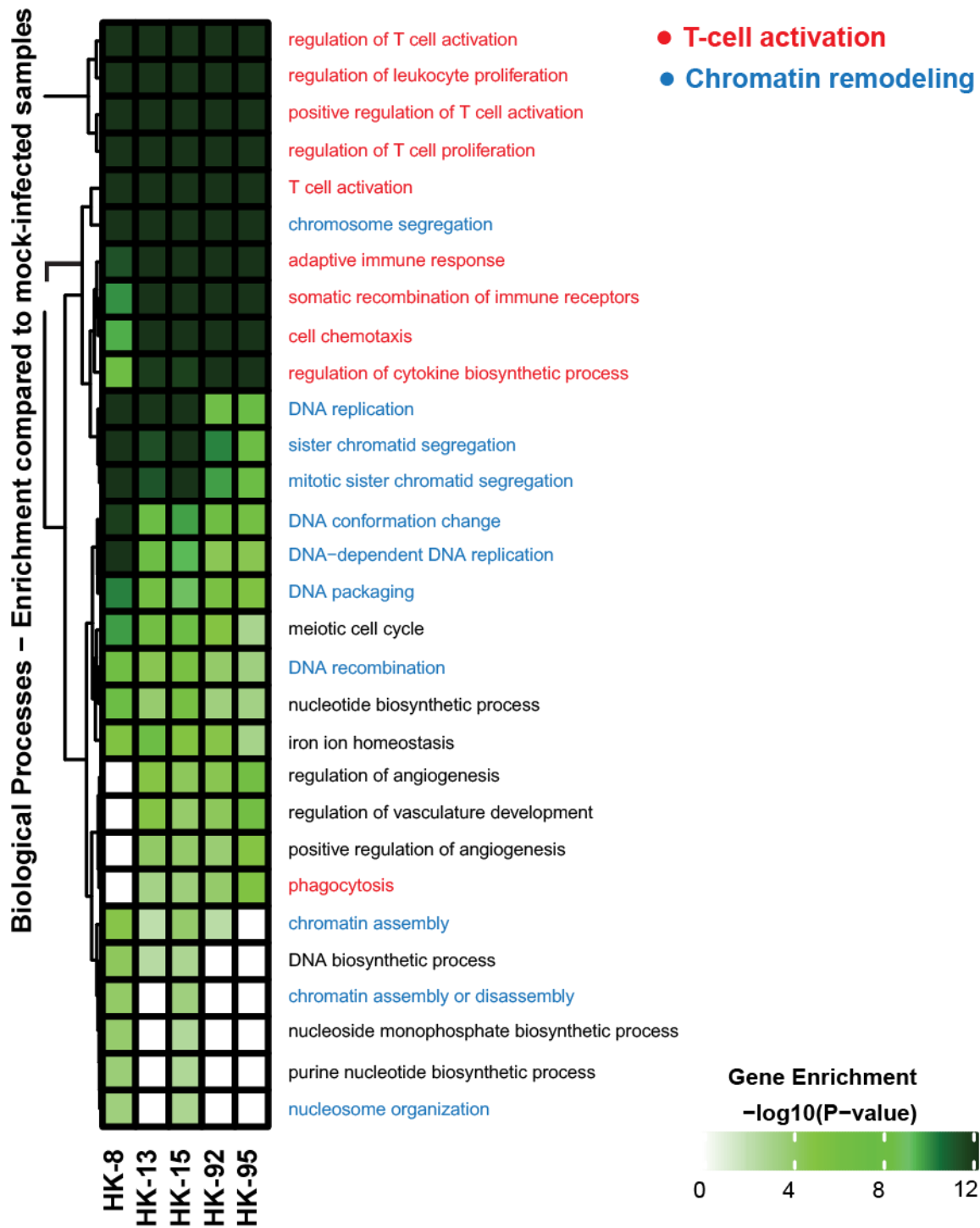


Figure 5

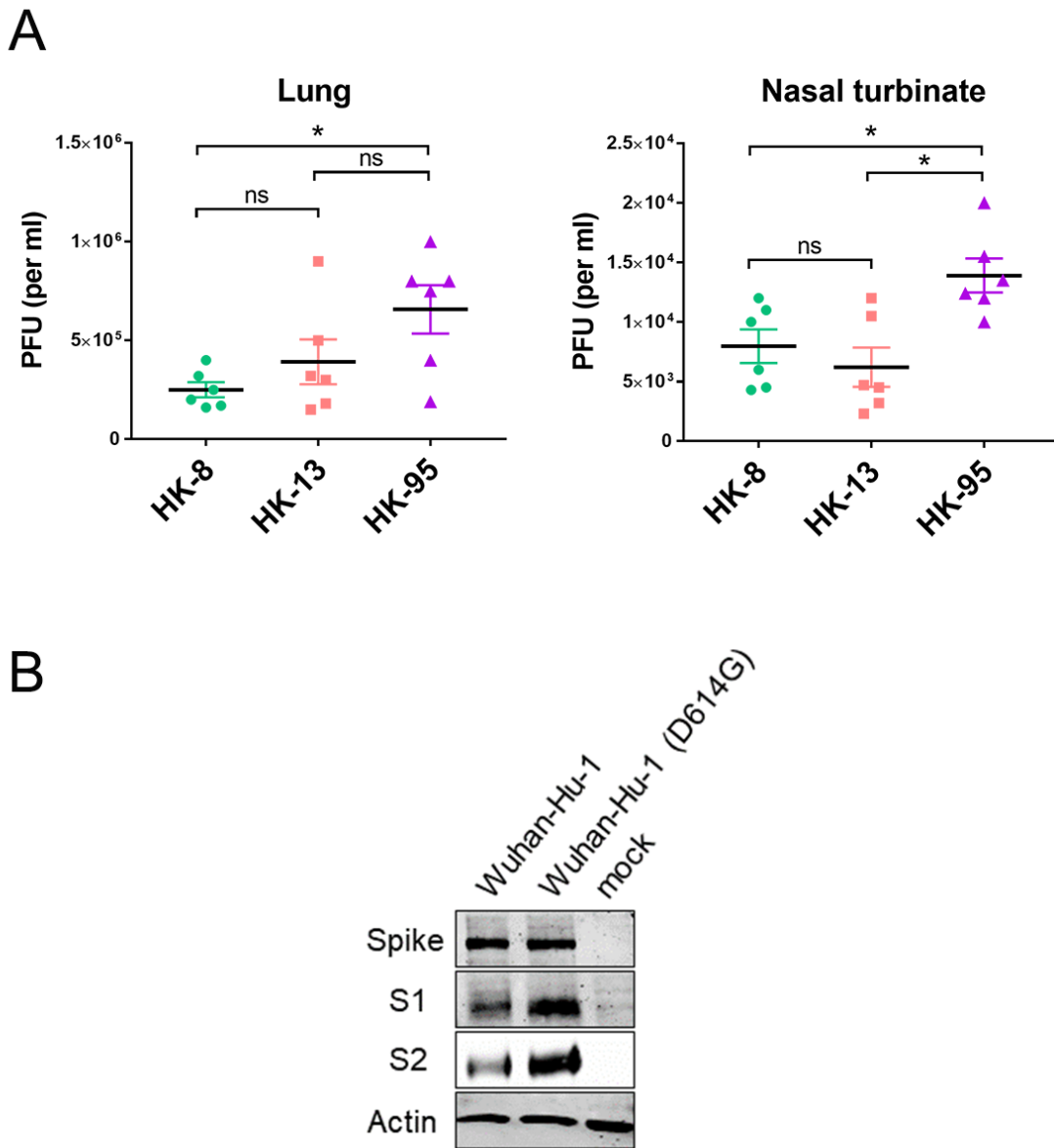


Table 1. Sequence diversity in SARS-CoV-2 isolates

SITE	Wuhan-Hu-1	8	13	15	92	95	AA	ORF	Occurrence frequency [§]
241	C	-	-	-	-	T	--	UTR	>50
1515	A	-	-	-	G	-	H417R	Orf1a	17
3037	C	-	-	-	-	T	--	Orf1a	>50
4093	C	-	-	-	C/T*	-	--	Orf1a	1
4899	A	-	-	-	A/G*	-	H1545R	Orf1a	0
5310	C	C/T*	-	-	-	-	T1682I	Orf1a	12
8092	C	T	-	-	-	-	--	Orf1a	7
9223	C	-	-	-	T	-	--	Orf1a	20
10981	G	-	-	G/T#	-	-	--	Orf1a	0
11083	G	T	-	-	T	-	L3606F	Orf1a	>50
12565	G	-	-	-	T	-	Q4100H	Orf1a	0
14408	C	-	-	-	-	T	P314L	Orf1b	>50
14805	C	-	-	-	T	-	--	Orf1b	>50
17247	T	-	-	-	C	-	--	Orf1b	>50
17423	A	-	G	G	-	-	Y1319C	Orf1b	>50
20667	A	-	G	-	-	-	--	Orf1b	1
21137	A	A/G**	-	-	-	-	K2557R	Orf1b	33
23403	A	-	-	-	-	G	D614G	S	>50
26144	G	-	-	-	T	-	G251V	Orf3a	>50
27920	C	-	C/T#	-	-	-	--	Orf8	1
28854	C	-	T	T	-	-	S194L	N	>50

* Reported variants with variant frequency between 10% - 30%.

** Reported variants with variant frequency 10% or below

Variant frequency varies between samples derived from the same isolate

§ Data were retrieved on August 6, 2020 from GenBank